ARTICLE OPEN

Check for updates

Flexible and transparent thin-film light-scattering photovoltaics about fabrication and optimization for bifacial operation

Soo-Won Choi [1,2], Jae-Ho Park[3], Ji-Woo Seo[1,2], Chaewon Mun[1], Yonghun Kim[1], Pungkeun Song[2 ✉], Myunghun Shin [4 ✉] and Jung-Dae Kwon[1,5 ✉]

Flexible and transparent thin-film silicon solar cells were fabricated and optimized for building-integrated photovoltaics and bifacial operation. A laser lift-off method was developed to avoid thermal damage during the transfer of light-scattering structures onto colorless polyimide substrates and thus enhance front-incidence photocurrent, while a dual n-type rear window layer was introduced to reduce optical losses, facilitate electron transport for rear incidence, and thus enhance performance during bifacial operation. The introduction of the window layer increased the rear-to-front power conversion efficiency ratio to ~86%. The optimized bifacial power conversion efficiency for front and rear irradiances of 1 and 0.3 sun, respectively, equaled 6.15%, and the average transmittance within 500–800 nm equaled 36.9%. Additionally, the flexible and transparent solar cells fabricated using laser lift-off exhibited good mechanical reliability (i.e., sustained 500 cycles at a bending radius of 6 mm) and were therefore suitable for building-integrated photovoltaics.

INTRODUCTION

The use of fossil energy sources significantly contributes to climate change and air pollution through the emission of volatiles such as carbon and nitrogen oxides[1,2]. Among the renewable substitutes for fossil fuels (e.g., sunlight, solar heat, wind, and wave energy), photovoltaic (PV) energy has proven to be economically feasible and currently has the largest market share. Electricity, which is the most commonly used form of energy in modern society, suffers from the highest energy losses upon transmission[3–5]. Building-integrated photovoltaics (BIPVs) can be an efficient electricity source, as they can be integrated into building rooftops, exterior walls, and windows to secure a direct energy supply[6–9]. In addition, bifacial solar modules based on the BIPV technology have found potential applications, e.g., vertical bifacial modules for PV power plants or sound barriers can complement the power generation characteristics of conventional tilted modules[10], while transparent bifacial modules installed in agrivoltaics or green-houses can concurrently produce crops and electricity[11,12]. As the exterior of modern buildings often features glass surfaces curved according to various esthetic designs, BIPV systems require flexible or bendable transparent solar cells (TSCs).

Various polymer materials such as poly (ethylene terephthalate), poly (ethylene 2,6-naphthalate), and colorless polyimide (CPI)[13–15] have been used as substrates for flexible and bendable solar cells. Among the polymer substrates, CPI has been widely used in flexible solar cells because of its relatively high melting point and glass transition temperature as well as superior mechanical and optical properties that are retained even after thermal processing[16,17]. Flexible TSCs can be constructed using thin-film materials such as copper indium gallium selenide (CIGS),

dye-sensitized, organic, and perovskite solar cells, and hydrogenated amorphous silicon (a-Si:H)[13–15,18,19], among which a-Si:H offers the advantages of solar cell stability, nontoxicity, low cost, and suitability for large-scale production[7,8]. In particular, the a-Si:H layer can be deposited using plasma-enhanced chemical vapor deposition (PECVD) at temperatures tolerated by CPI substrates[20], while the high visible-light absorption coefficient of a-Si:H[21] enables efficient power generation using indoor light. The a-Si:H-based solar cells reported to date can be classified as opaque or transparent. For opaque cells, stabilized power conversion efficiencies (PCEs) of 10.2% (single-junction structure[22]) and 14.0% (triple-junction structure[23]) have been reported, while PCE–average transmittance (T_{avg}) pairs of 6.9%–23.6%[24] and 3.4%–33.0%[25] have been reported for transparent cells. Flexible thin-film opaque silicon solar cells with single[26] and tandem structures[27] on PEN substrates have been shown to exhibit a PCE of 8.8% and a stabilized PCE of 9.8%, respectively, with PCE–T_{avg} pairs of 3.0%–40% and 4.93%–34.2% reported for transparent cells based on Kapton[28] and PEN substrates[14], respectively.

Several technical issues must be resolved to manufacture high-performance flexible TSCs on CPI substrates. The ability of thin-film solar cells to absorb light can generally be increased using light-scattering structures, which, however, are difficult to create on flexible substrates. As CPI substrates easily generate surface stress due to thermal expansion, the creation of a-Si:H absorption layers on surfaces with irregularities, e.g., on light-scattering (textured) structures, tends to favor defect formation. In addition, although TSCs can be operated in bifacial mode[7,29], i.e., can generate electricity using both front and rear incident light, most thin-film TSCs have been optimized for front

[1]Surface & Nano Materials Division, Korea Institute of Materials Science, Changwon, Gyeongnam 51508, Republic of Korea. [2]Department of Materials Science and Engineering, Pusan National University, Busan 46241, Republic of Korea. [3]Cell R&D Team, Hanhwa QCells, 202 Sansusandan 2-ro, Lwol-myeon, Jincheon-gun, Chungcheongbuk-do 27816, Republic of Korea. [4]School of Electronics and Information Engineering, Korea Aerospace University, Goyang, Gyeonggi 10540, Republic of Korea. [5]Department of Advance Materials Engineering, University of Science and Technology (UST), 217 Gajeong-ro, Yuseong-gu, Daejeon 34113, Republic of Korea. ✉email: pksong@pusan.ac.kr; mhshin@kau.ac.kr; jdkwon@kims.re.kr
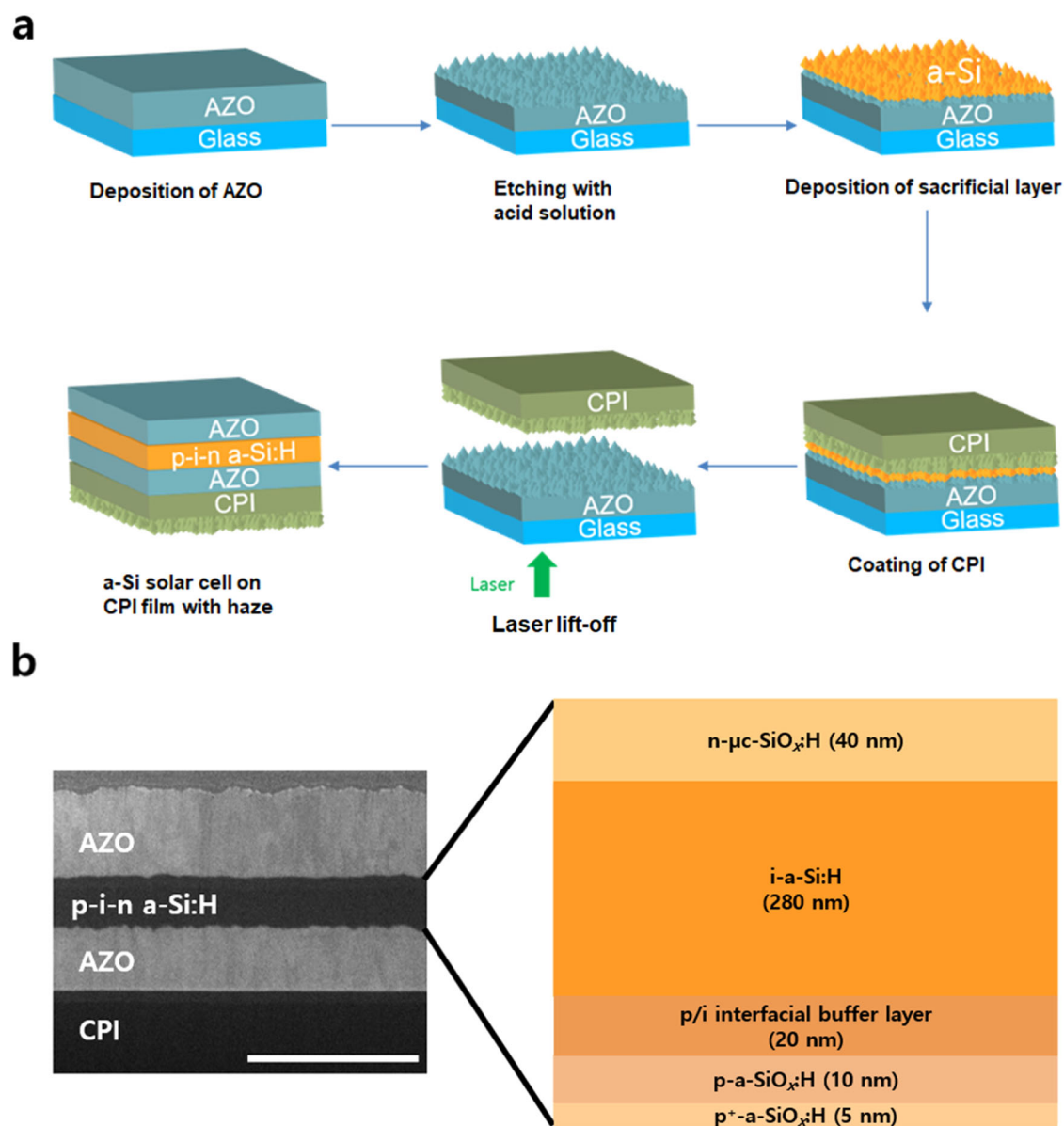
Fig. 1 CPI and solar cells fabrication. a Schematic fabrication of colorless polyimide (CPI) films and flexible hydrogenated amorphous silicon (a-Si:H) solar cells. **b** Cross-sectional scanning electron microscopy image and schematic layered structure (thickness) of p-i-n a-Si:H in fabricated solar cells, scale bar is 1 μm.

incidence and therefore feature large differences between front- and rear-incidence PCEs[30–33].

Herein, we fabricated ultra-thin (~20 μm) flexible transparent a-Si:H solar cells suitable for BIPV systems (Fig. 1). The proposed device was integrated with a light-scattering structure at the CPI substrate surface. A variety of light-scattering techniques such as front electrode texturing, optical structure imprinting on substrates, silver nanowire meshing, and light-scattering structure transfer using replication can be used for thin-film solar cells[34–40]. Among these methods, we chose laser lift-off (LLO) transfer because of its low susceptibility to thermal or chemical influences and the resulting ease of application to flexible substrates. The light-scattering structure produced by adjusting the etching time of aluminum-doped zinc oxide (AZO) was transferred to the CPI substrate, and a transparent a-Si:H solar cell was integrated on the flat substrate surface. Fabricating the cell on the opposite surface of the light-scattering structure can exploit the light-scattering properties and reduce the number of

defects in the cell by reducing the surface stress induced during a-Si:H deposition. We also introduced an n-type rear layer to reduce optical losses for rear incidence and optimized this layer using optical reflectance simulations. The bandgap structure of the n-type rear layer was engineered to facilitate electron transport and thus provide an advantage for rear irradiance. Finally, we investigated the morphology of the transferred CPI (T-CPI) film and the performance of T-CPI-based transparent a-Si:H solar cells, additionally examining the mechanical properties of flexible solar cells using a bending test.

RESULTS AND DISCUSSION
Characteristics of CPI films with light-scattering structures
The CPI film was separated from the glass substrate using the LLO method, according to which the sacrificial a-Si:H layer was removed by the laser through vaporization (LLO step, Fig. 1a). Thus, laser power had to be optimized to minimize optical losses,
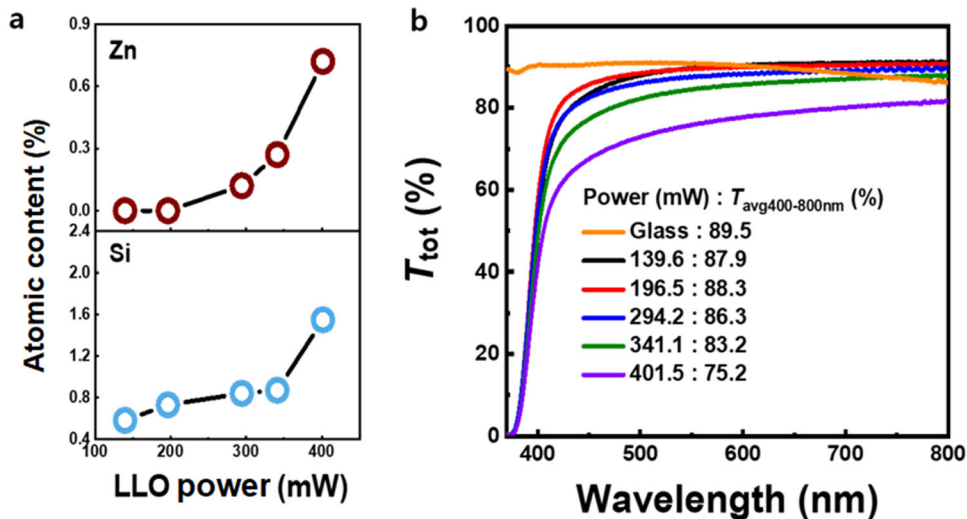
Fig. 2 Film quality with laser lift-off (LLO) power. Effects of LLO power on **a** residual Si and Zn contents and **b** total transmittance curves of CPI films.

that is, the CPI film had to be removed without damaging the substrate or leaving a-Si:H residues (which can absorb or reflect incident light to cause unwanted optical losses)[41]. Figure 2a shows the contents of residual elements (determined using energy-dispersive X-ray spectroscopy, Supplementary Fig. 1) on the surface of separated CPI films as a function of LLO power, revealing that sacrificial layer removal started at 139.5 mW. As LLO power increased from 139.6 to 401.5 mW, the content of Si and Zn residues increased from 0.6 to 1.6 wt% and from 0 to 0.7 wt%, respectively. The total transmittance of CPI films as a function of LLO power is given in Fig. 2b. CPI films produced at 139.6 and 196.5 mW exhibited relatively low residue amounts and featured T_{avg} values of 87.9% and 88.3% in the range of 400–800 nm, respectively. These transmittances were similar to that of soda–lime glass (Central Glass Co., $T_{avg} = 89.5\%$). With an increase in LLO power to 294.2, 341.1, and 401.5 mW, T_{avg} decreased to 86.3, 83.2, and 75.2%, respectively. We assumed that the vaporized amorphous Si of the sacrificial layer was redeposited on the CPI surface under the condition of high LLO power. Similarly, at high LLO power, Zn in AZO could also be vaporized to leave a residue on the CPI surface. At LLO powers above 196.5 mW, the CPI films exhibited high optical losses due to residual Si and Zn. Thus, T-CPI films and TSCs on T-CPI substrates we fabricated at an LLO power of 196.5 mW.
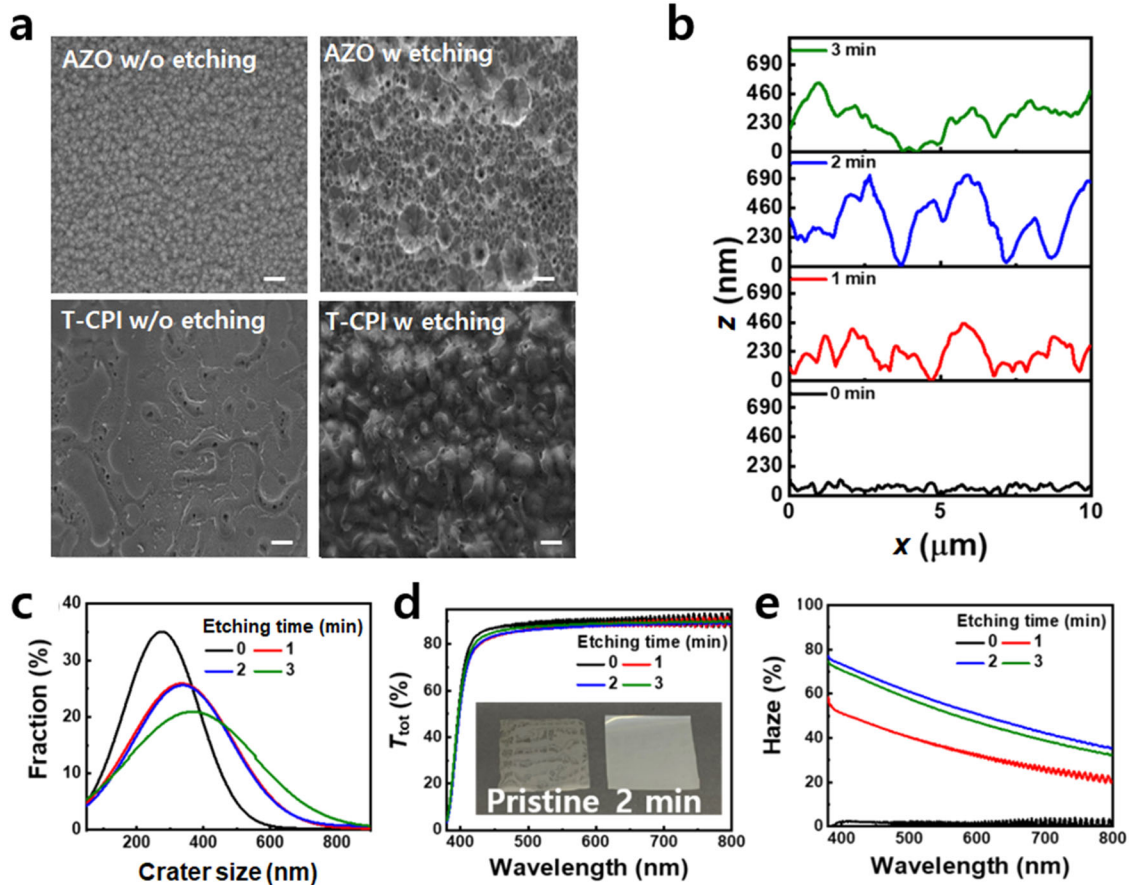
The field-emission scanning electron microscopy images in Fig. 3a show the surface morphologies of AZO and CPI produced with and without wet etching, revealing that the AZO surface structure was well transferred to the CPI. Notably, the AZO surface became rough as craters were formed by etching; for the T-CPI produced using etching, we observed a convexo-concave surface and the transcription of craters on the etched AZO surface. The surface morphology of this T-CPI was quantitatively analyzed using the surface line scanning profiles and lateral size distributions derived from the atomic force microscopy images in Supplementary Fig. 2. Figure 3b shows that the overall height difference between peaks and valleys increased up to an etching time of 2 min and then decreased at 3 min. The average root-mean-square roughness (R_a) for etching times of 0, 1, 2, and 3 min was 40.9, 85.4, 121.1, and 117.4 nm, respectively (Supplementary Fig. 3). The lateral average size and dispersion of surface craters increased with etching time (Fig. 3c). The results in Fig. 3b, c can be explained by the two-step wet-etching mechanism of AZO. According to this mechanism, etching starts at the grain boundaries of AZO (where the dangling bonds are concentrated)

and forms craters, the height, and width of which increase with time. Subsequently, when AZO decomposition involves the entire surface, the crater lateral size (width) increases with decreasing height[35,37,42].

Figure 3d shows the total transmittance of T-CPI films as a function of AZO etching time. The T_{avg} in the range of 400–800 nm at 0, 1, 2, and 3 min was determined as 88.3, 86.4, 86.2, and 86.3%, respectively. Thus, etching time had no significant effect on CPI film transmittance and, hence, optical losses. In addition, the small transmittance loss indicated that the LLO process enabled the good physical separation of the CPI substrate without thermal or chemical degradation. The haze values (light-scattering degree) in the 400–800 nm range at etching times of 0, 1, 2, and 3 min were 1.0, 33.5, 51.9%, and 48.6%, respectively (Fig. 3e). Mie scattering can occur in three-dimensional surface structures[43]. The highest haze value was obtained at the greatest height and width of craters on the AZO surface, and the results of Fig. 3b–e indicate that the T-CPI produced using an etching time of 2 min was most optically suitable for TSCs. Moreover, the production of this T-CPI could be upscaled to dimensions of 140 mm × 140 mm (Supplementary Fig. 4).

Properties of flexible thin-film silicon TSCs

We fabricated TSCs on T-CPI substrates (Fig. 1) and characterized them in terms of current density (J), voltage (V), and external quantum efficiency (EQE). TSCs prepared on the surface of the T-CPI with a light-scattering structure could not be operated or suffered from severe fill factor (FF) and open-circuit voltage (V_{OC}) losses; therefore, the TSCs had to be prepared as shown in Fig. 1a. We compared the PV performances of cells using both front and rear irradiance, with the detailed PV parameters (averages) shown in Table 1 and Fig. 4. Owing to the transferred light-scattering structures on the CPI, the corresponding short-circuit current densities ($J_{SC} = 9.34$, 9.83, and 9.37 mA/cm^2 for etching times of 1, 2, and 3 min, respectively; J–V curves) exceeded that of the planar CPI (9.15 mA/cm^2 without etching; J–V curve), whereas the corresponding V_{OC} and FF values were similar. As expected from the results of Fig. 3, the highest performance was obtained at 2 min, in which case light-scattering improved the photogenerated current to the greatest extent. EQE data also showed that the light-scattering properties of T-CPI improved light absorption over the entire wavelength range (integrated $J_{SC} = 9.81$, 10.10, 10.63, and 10.18 mA/cm^2 for etching times of 0, 1, 2, and 3 min,

Fig. 3 Structural and optical properties of transferred CPI (T-CPI). a Field-emission scanning electron microscopy images (10 μm × 10 μm) of pristine and etched aluminum-doped zinc oxide (AZO) surfaces and T-CPI film surfaces prepared using pristine and etched AZO, scale bar is 1 μm. **b** Line scanning profiles of T-CPI films prepared using different AZO etching times to transfer surface morphology. **c** Gaussian distribution of transferred crater size in lateral direction of each T-CPI. **d** Total transmittance curves and **e** wavelength-dependent optical haze of T-CPI films prepared using different etching times.

Table 1. Effects of etching time (ET) and irradiance mode (F: front irradiance, R: rear irradiance) on cell performance parameters (averages and standard deviations determined for eight cells).

ET (min)	Mode	V_{OC} (V)	J_{SC} (mA/cm^2)	FF (%)	PCE (%)
0	F	0.824 (± 0.010)	9.11 (± 0.07)	64.8 (± 0.5)	4.87 (± 0.05)
	R	0.831 (± 0.002)	6.59 (± 0.05)	57.2 (± 0.6)	3.13 (± 0.05)
1	F	0.827 (± 0.010)	9.35 (± 0.07)	66.3 (± 0.3)	5.12 (± 0.03)
	R	0.818 (± 0.003)	7.24 (± 0.27)	58.9 (± 2.3)	3.49 (± 0.08)
2	F	0.827 (± 0.010)	9.81 (± 0.06)	65.7 (± 0.5)	5.34 (± 0.02)
	R	0.822 (± 0.008)	7.28 (± 0.06)	60.6 (± 0.5)	3.63 (± 0.04)
3	F	0.814 (± 0.010)	9.43 (± 0.04)	66.5 (± 0.8)	5.10 (± 0.08)
	R	0.829 (± 0.002)	7.10 (± 0.20)	54.7 (± 2.6)	3.22 (± 0.14)

respectively). As a result, the T-CPI with the highest extent of light-scattering exhibited a PCE of 5.34% for front-side irradiance, which exceeded that of the planar CPI by 9.7%. However, as the light-scattering structure changes the path of incident light to increase absorbance, it can reduce visibility when used in windows. Therefore, future works should establish an optimal trade-off between efficiency and visibility for PV windows.

As mentioned above, TSCs have a bifacial structure and can therefore generate electricity by receiving light from both the front and the rear. This ability allows one to utilize both outdoor sunlight and indoor light sources when TSCs are used as BIPV

windows, while outdoor sunlight and albedo light can be utilized when TSCs are used as BIPV vertical walls[10–12]. Thus, performance in the case of rear-side irradiance is also important. The rear-side properties of our cells are shown in Fig. 4c, which presents $J–V$ characteristics. The observed J_{SC} values increased with the use of T-CPI for rear irradiance, but the rear-side J_{SC} values were lower than the corresponding front-side values (integrated J_{SC} for rear-side irradiance: 7.47, 7.81, 7.84, and 7.78 mA/cm^2 for etching times of 0, 1, 2, and 3 min, respectively). In particular, the EQE was low in the short-wavelength range of <550 nm, in which a-Si:H cells absorb to generate power.
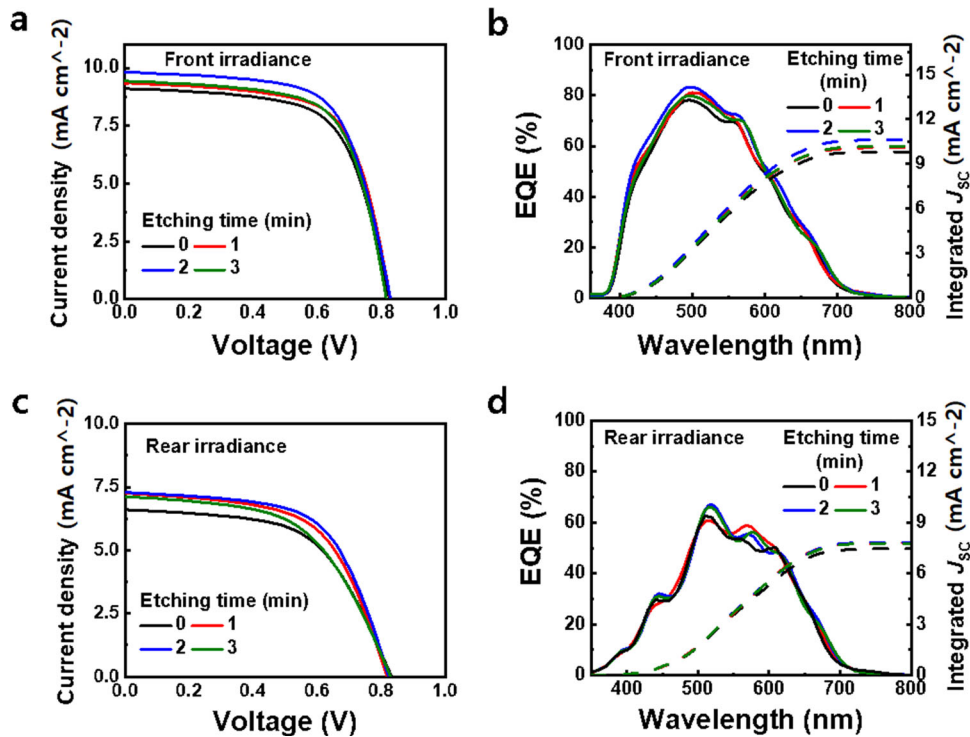
Fig. 4 Flexible TSCs characteristics. Effects of etching time on **a, c** current density–voltage (J–V) curves and **b, d** external quantum efficiency (EQE) spectra and integrated short-circuit current densities (J_{SC}) of transparent solar cells (TSCs) fabricated using T-CPI films: **a, b** front-side and **c, d** rear-side irradiance.

## Effects of incidence direction on optical properties of flexible TSCs

The optical losses in the rear side of cells were assumed to be the main cause of the low J_{SC} for rear irradiance; i.e., the reflection from the rear was believed to result in direct photocurrent losses, while absorption in the n-layer could not contribute to the photocurrent. Thus, we measured the total transmittance and reflectance of the cell on the T-CPI with 2-min etching for different light incidence directions (Fig. 5a, b). The front and rear transmittances were almost the same, but the rear reflectance exceeded the front reflectance in the short-wavelength range of <600 nm, which caused a reduction in J_{SC} for rear irradiance.

Therefore, we introduced an n-type rear (n-rear) window layer to reduce optical losses for rear illumination. When the oxygen content of the n-type hydrogenated microcrystalline silicon oxide (n-μc-SiO_x:H) layer increases, so does the bandgap energy, which can reduce light absorption losses. In addition, the refractive index of the n-μc-SiO_x:H layer decreases with increasing oxygen content[44], which provides a handle for adjusting rear-side reflectance. The oxygen content can be controlled by the gas flow ratio of CO_2 to SiH_4 (CO_2/SiH_4) during the n-μc-SiO_x:H layer deposition. The growth conditions for 40-nm-thick n-μc-SiO_x:H layers were optimized by increasing the CO_2/SiH_4 from 0.6 to 1.8 (i.e., increasing the oxygen content). The n-μc-SiO_x:H layer deposited at the CO_2/SiH_4 of 1.8 ($C_{1.8}$) exhibited a bandgap larger than that of the existing pristine n-μc-SiO_x:H layer deposited at the CO_2/SiH_4 of 0.6 ($C_{0.6}$). Supplementary Table 1 compares the bandgap characteristics of the two n-μc-SiO_x:H layers with those of the intrinsic absorber layer. The n-rear window layer was designed with two n-layers ($C_{0.6}$ and $C_{1.8}$) to reduce optical losses for rear irradiance. To analyze and design reflectance at the rear, we measured the refractive index (n) and extinction coefficient (k) of each cell layer using a spectroscopic ellipsometer. Supplementary Fig. 5 shows that the refractive indices of $C_{1.8}$ and $C_{0.6}$ were between those of AZO and i-a-Si:H

layers, suggesting that reflectivity can be reduced through design optimization. Using the optical parameters of Supplementary Fig. 5, we simulated optical reflectance for the rear side[45]. The optical reflectance simulation using optical admittance is described in S1–S5 in Supplementary Method. To optimize the rear n-layer, we also conducted a rear-side reflectance simulation of TSCs for layers with various oxygen doping degrees and thickness ratios (Supplementary Fig. 6). As shown in Fig. 5c, the reflectance of the $C_{1.8}$ layer (40 nm) in the short-wavelength range (400–600 nm) was similar to that of the dual n-rear window layer ($C_{0.6}/C_{1.8}$ of 10/30 nm) and lower than that of the $C_{0.6}$ layer (40 nm). The thickness of the n-rear window layer ($C_{0.6}/C_{1.8}$ of 10/30 nm) was also optimized using optical reflectance simulation, and the measured reflectance was in good agreement with the simulation results (Fig. 5c, d).

Optimization of flexible TSCs for bifacial operation

The PV performance of TSCs with an n-rear window layer for front and rear irradiances is shown in Fig. 6, and the related PV parameters (average values) are listed in Table 2. For front irradiance, the cells exhibited similar V_{OC} values, whereas J_{SC} and FF values slightly decreased in the case of a wide-bandgap n-layer. Specifically, for $C_{0.6}$, $C_{1.8}$, and $C_{0.6}/C_{1.8}$, the J_{SC} values of Fig. 6b were 9.83, 9.69, and 9.43 mA/cm², respectively, while the respective FF values equaled 65.6, 57.4, and 62.9%. In the case of the n-rear window layer ($C_{0.6}/C_{1.8}$), PCE reduction was much smaller than for $C_{1.8}$ compared with $C_{0.6}$. Figure 6b shows that when the n-rear window layer was used, PCE improvement for rear incidence was much greater than the PCE reduction for front incidence. The J–V curve recorded for rear incidence showed that both J_{SC} and PCE greatly increased to 8.83 mA/cm² and 4.24%, respectively. The EQE for rear irradiance also increased upon the introduction of the n-rear window layer ($C_{0.6}/C_{1.8}$; Fig. 6c), with integrated J_{SC} values of 7.84, 8.62, and 9.41 mA/cm² obtained for $C_{0.6}$, $C_{1.8}$, and $C_{0.6}/C_{1.8}$, respectively.
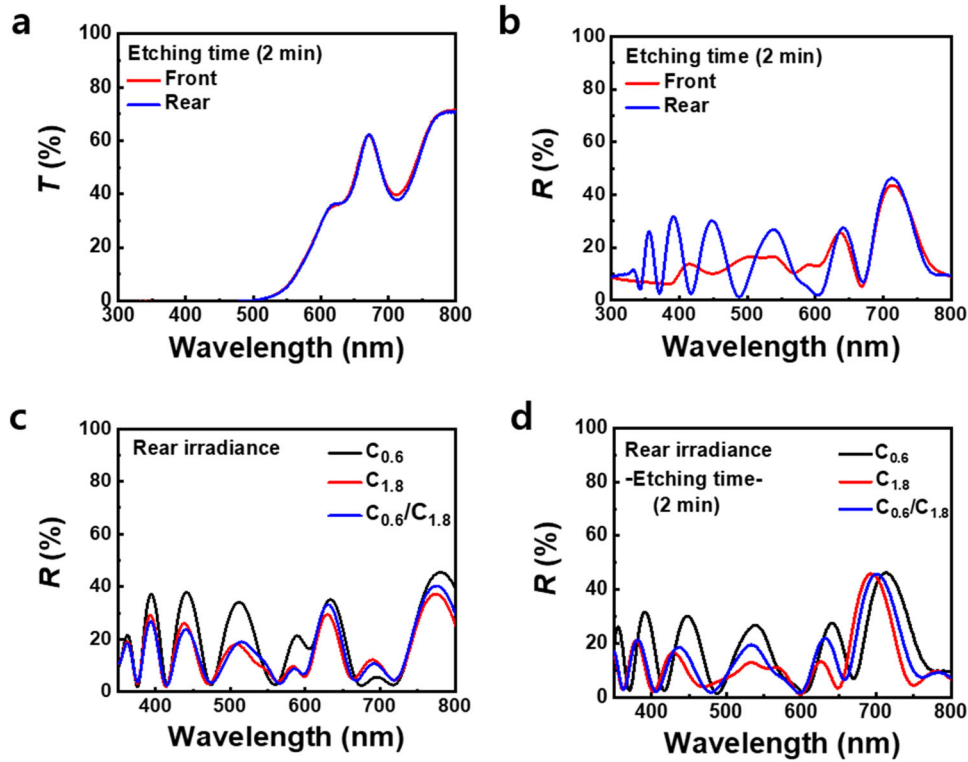
Fig. 5 Optical properties with direction of irradiance. a Transmittance and **b** reflectance spectra of TSC fabricated on T-CPI film with etching time of 2 min (front- and rear-side irradiance). **c** Simulated and **d** experimental rear-side reflectance spectra of TSCs prepared on T-CPI. Experimental spectra refer to etching time of 2 min and three different structures ($C_{0.6}$, $C_{1.8}$, and $C_{0.6}/C_{1.8}$) of n-type hydrogenated microcrystalline silicon oxide (n-μc-SiO$_x$:H).
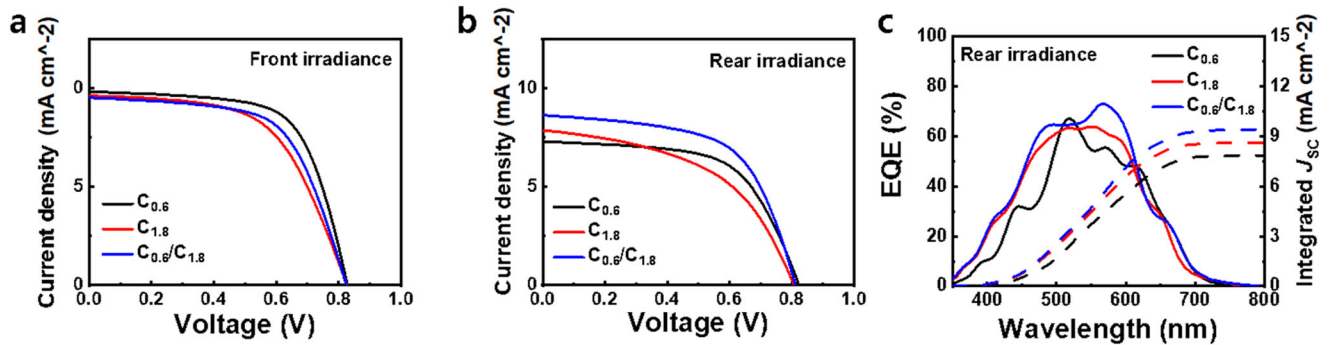
Fig. 6 Flexible TSCs characteristics with rear-window layers. Effects of three different structures ($C_{0.6}$, $C_{1.8}$, and $C_{0.6}/C_{1.8}$) of n-μc-SiO$_x$:H on *J–V* curves of TSCs deposited on T-CPI with etching time of 2 min for cases of **a** front-side and **b** rear-side irradiance. **c** EQE spectra and integrated J_{SC} values of above cells for case of rear-side incidence.

The increase in EQE upon going from $C_{0.6}$ to $C_{1.8}$ and $C_{0.6}/C_{1.8}$ in the case of rear irradiance (Fig. 6c) was mainly due to the concomitant absorbance enhancement (Supplementary Fig. 7) caused by the reduction of reflection losses (Fig. 5d). However, given the similar absorbance values for $C_{1.8}$ and $C_{0.6}/C_{1.8}$, the reduced reflectance (Fig. 5d) alone was insufficient to explain the higher integrated and measured J_{SC} values of $C_{0.6}/C_{1.8}$ compared to those of $C_{1.8}$. The conduction band offset (ΔE_C) at the i/n-interface due to the wide-bandgap n-layer acted as an energy barrier impeding electron transport to this layer. In the case of rear irradiance, carrier recombination losses can increase with increasing energy barrier height and width because the carriers are mostly generated near the i/n-interface. The energy band diagram of this interface for different n-layers is illustrated in Supplementary Fig. 8, which was configured using the

parameters in Supplementary Table 1. In Supplementary Fig. 8, the ΔE_C of $C_{0.6}/C_{1.8}$ is between those of $C_{1.8}$ (0.335 eV) and $C_{0.6}$ (0.22 eV) because of the band-bending effect of the electric field. Therefore, for rear irradiance, carrier collection at $C_{0.6}/C_{1.8}$ was better than that at $C_{1.8}$, which resulted in the largest increases in J_{SC} and PCE observed for $C_{0.6}/C_{1.8}$.

However, the rear-incidence J_{SC}, FF, and PCE values were still lower than the corresponding front-incidence values, possibly because in a-Si:H, hole mobility is lower than electron mobility. Specifically, the holes, which are mostly generated near the rear (by rear irradiance), need to be gathered in the p-layer of the front but can easily recombine during transport to this layer[46,47]. Another reason is the presence of ΔE_C causing carrier recombination at the interface. The ΔE_C of $C_{0.6}$ was lower than that observed in other cases, and the FF values, therefore,

Table 2. Performance parameters (averages and standard deviations determined for eight cells) of T-CPI cells prepared using an etching time of 2 min and different n-μc-SiOx:H formation conditions (F: front irradiance, R: rear irradiance, B: bifacial irradiance).

n-μc-SiOx:H	Mode	V_{OC} (V)	J_{SC} (mA/cm^2)	FF (%)	PCE (%)
C$_{0.6}$	F	0.827 (± 0.010)	9.81 (± 0.06)	65.7 (± 0.5)	5.34 (± 0.02)
	R	0.822 (± 0.008)	7.28 (± 0.06)	60.6 (± 0.5)	3.63 (± 0.04)
	B	0.837 (± 0.006)	11.62 (± 0.04)	58.0 (± 0.6)	5.65 (± 0.04)
C$_{1.8}$	F	0.826 (± 0.011)	9.61 (± 0.11)	57.5 (± 1.6)	4.57 (± 0.14)
	R	0.806 (± 0.011)	7.84 (± 0.36)	49.4 (± 1.3)	3.12 (± 0.09)
	B	0.831 (± 0.008)	12.29 (± 0.30)	53.8 (± 1.8)	5.49 (± 0.02)
C$_{0.6}$/C$_{1.8}$	F	0.824 (± 0.002)	9.51 (± 0.06)	61.9 (± 0.9)	4.85 (± 0.06)
	R	0.811 (± 0.001)	8.61 (± 0.07)	59.7 (± 0.7)	4.17 (± 0.08)
	B	0.833 (± 0.002)	12.30 (± 0.08)	60.1 (± 0.8)	6.15 (± 0.06)

increased in the order of C$_{1.8}$ < C$_{0.6}$/C$_{1.8}$ < C$_{0.6}$ for front irradiance (Fig. 6b).

According to Table 2, the rear-to-front PCE ratio for C$_{0.6}$/C$_{1.8}$ (86%) greatly exceeded that for C$_{0.6}$ (68%); therefore, the n-rear window layer of C$_{0.6}$/C$_{1.8}$ was expected to favor bifacial operation. For bifacial operation, 100-mW/cm^2 power (1 sun) was irradiated to the front, and 30-mW/cm^2 power (0.3 sun) was irradiated to the rear. Under this condition, the cell with C$_{0.6}$/C$_{1.8}$ exhibited the best performance (Fig. 7a), featuring a bifacial PCE of 6.15%, a T_{avg} of 36.9% in the wavelength range of 500–800 nm, and good flexibility (Fig. 7b). Notably, front and rear light powers of 1 and 0.3 sun, respectively, were used to measure bifacial efficiency. This condition is good for outdoor BIPV modules, but if the module is intended for use in the PV windows of conventional buildings, bifaciality under this irradiance condition should be carefully investigated and evaluated, as indoor light sources are generally much less powerful compared to outdoor albedo light.

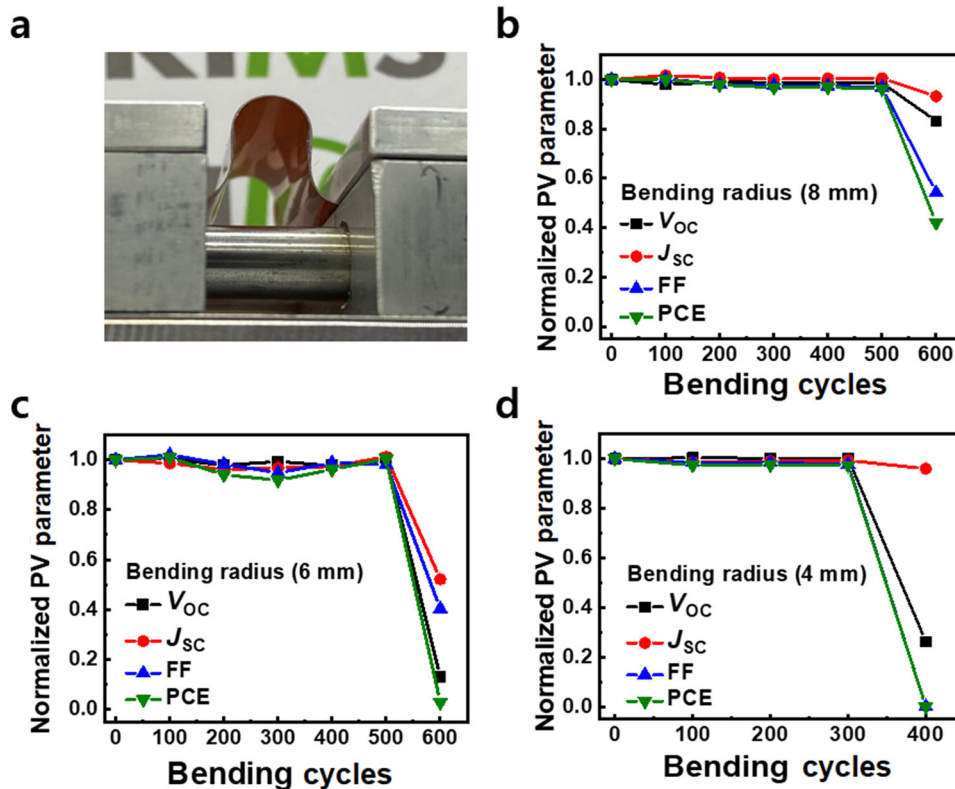## Flexibility and reliability of flexible TSCs

The mechanical properties of solar cells fabricated on flexible substrates are also important. The bifacial flexible TSCs manufactured using LLO exhibited very high mechanical reliability. The bending (application of tensile stress to cells on the inner radius surface) tests were repeated with different bending radii (R) using the method shown in Fig. 8a. Figure 8 shows the average (eight cells) normalized PV parameter changes upon bending, revealing that the cells could withstand 500 bending cycles at $R = 8$ and 6 mm, and 300 bending cycles at $R = 4$ mm. This performance is superior to that reported previously[14], in which case bending was performed for 350 cycles at $R = 14$ mm. We note that for the planar T-CPI without a light-scattering structure, the PCE will be lower than for the T-CPI with a light-scattering structure, whereas mechanical durability can be better (Supplementary Figs. 9a–c). The thermal stress in T-CPI can deteriorate the cell; when using LLO power, which is almost twice the normal laser power, we observed that the initial PCE and bending resistance were much worse than those achieved using optimized LLO power (Supplementary Fig. 9d). We believe that excessive LLO power causes thermal damage to the CPI, resulting in cell defect formation during fabrication and increasing vulnerability to bending stress. In the compressive bending test (stress applied on the outer radius surface), the cell endured up to 900 cycles at $R = 6$ mm (Supplementary Fig. 9e), as less displacement occurred in the case of compressive stress at the inner radius surface than in the case of tensile stress at the outer radius surface. Figure 8 shows that FF and V_{OC} mainly deteriorated upon continuous bending, and the PCE consequently decreased. The bending radius was negatively correlated with the degradation rate. This behavior was most likely due to the hard but brittle AZO being damaged upon repeated bending. Thus, we expect that the mechanical properties of TSCs

can be further improved through electrode optimization in the future. Additionally, we conducted the light soaking test, which is one of the most important reliability tests for a-Si:H solar cells due to silicon–hydride bonding. This test was conducted under AM 1.5 G 1-sun condition using a xenon lamp and light-emitting diodes (LEDs) as light sources. During the light soaking test (Supplementary Fig. 10), the performance parameters degraded and stabilized within 12 h. The PCE losses of ~10.1% and ~9.5% observed for xenon lamp and LEDs, respectively, were similar to those generally observed for a-Si:H solar cells.

Flexible and transparent a-Si:H solar cells were fabricated on CPI substrates with integrated light-scattering structures formed by etching AZO and transferring it to CPI substrates through the LLO process. By optimizing the LLO power, we achieved a high T_{avg} (88.3%, similar to the value of 89.5% obtained for the glass substrate) for the CPI substrates. The degree of light-scattering in T-CPI films could be controlled by varying the AZO etching time. Under optimal AZO etching conditions, a high haze value of 51.9% was achieved without any loss in T-CPI substrate transmittance. When the transparent a-Si:H solar cells were fabricated on optimized T-CPI substrates, the average J_{SC} and PCE improved from 9.11 to 9.81 mA/cm^2 and from 4.87 to 5.34%, respectively, for front incidence but were as low as 7.28 mA/cm^2 and 3.63% for rear incidence, respectively. Thus, a big difference in the performance of front and rear incidences was observed. Based on reflectance simulation, we introduced an optimized n-rear window layer. The dual n-rear window layer (C$_{0.6}$/C$_{1.8}$) decreased optical reflection losses and facilitated electron transport at the interface, reducing carrier recombination losses for rear irradiance. Therefore, the optimized cell exhibited the best average J_{SC} (9.51/8.61 mA/cm^2) and PCE (4.85/4.17%) for front/rear incidence. This cell was optimized for bifacial operation, such that the best PCE of 6.15% was obtained under 1-sun front and 0.3-sun rear irradiance conditions, maintaining a T_{avg} of 36.9%, and the rear PCE increased to 86% of the front PCE. In addition, the fabricated flexible solar cells exhibited very high mechanical reliability, sustaining 500, 500, and 300 bending cycles at $R = 8$, 6, and 4 mm, respectively. The methods presented herein can be used for the development of high-performance flexible BIPVs and exhibit the following advantages: (i) various light-scattering structures can be transferred to flexible substrates without serious thermal damage, (ii) the rear window layer can reduce both optical and electrical losses for bifacial operation, (iii) the cells will have reliable resistance to bending, and (iv) various absorber materials (thin-film silicon, CIGS, organic solar cells, and perovskite solar cells) can be used. The discovery of an advanced n-rear window layer capable of reducing ΔE_C should facilitate the development of bifacial TSCs with the same performance for front and rear incident light. The use of flexible and transparent electrodes
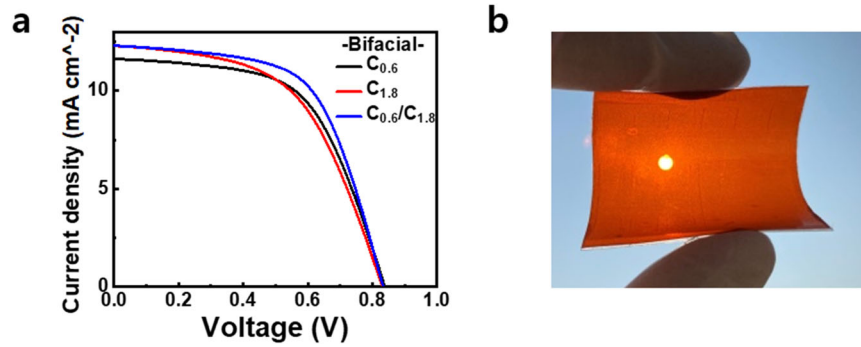
Fig. 7 Bifacial photovoltaics. a Bifacial J–V characteristics of TSCs fabricated on T-CPI with $C_{0.6}$, $C_{1.8}$, and $C_{0.6}/C_{1.8}$ structures and **b** representative image of flexible TSC.

Fig. 8 Mechanical durability of flexible TSCs. a Image showing setup used for repeated bending of flexible TSCs. Effects of repeated bending at bending radii of **b** 8, **c** 6, and **d** 4 mm on normalized photovoltaic (PV) device parameters averaged over eight cells.

superior to AZO is also expected to further improve the mechanical stability of flexible TSCs.

METHODS

Fabrication of CPI films and TSCs

The fabrication of CPI films is illustrated in Fig. 1a. An approximately 2-μm-thick AZO film was deposited on a 1.8-mm-thick soda-lime glass slide (50 mm × 50 mm) using a direct-current (DC) pulse magnetron sputtering system at 150 °C and 1000 W. The deposited AZO film was etched using a dilute acid solution (2 vol% nitric acid and 1.5 vol% acetic acid in deionized water) to form a light-scattering (textured) structure whose roughness could be tuned by varying the etching time (0, 1, 2, and 3 min). A thin (~100 nm) a-Si:H sacrificial layer was deposited on textured AZO using PECVD. The CPI film was spin-coated (at 400 rpm for 90 s) on the a-Si:H sacrificial layer and annealed (at 350 °C for 4 h)

using an IPI-C solution (5000 cps, solid content = 18.5 wt%). CPI film thickness was adjusted to ~20 μm. Finally, the CPI film was removed by removing the a-Si:H sacrificial layer using a diode-pumped solid-state (DPSS) LLO process. The DPSS laser employed a neodymium-doped yttrium orthovanadate (Nd:YVO$_4$) gain medium and operated at a wavelength of 532 nm. The laser process was conducted using a laser scribing machine (KORTherm Science Co.; emitted pulse duration ≈ 40 ns, frequency = 120 kHz), and the laser output power was adjusted by changing the fine-tuned external attenuator. In the LLO process, the laser pulse was vertically incident on the glass side, and single-time laser scanning was conducted using a galvanometer scanner at an optimized rate of 750 mm/s. Under these conditions, a ~20-μm beam diameter with a spot overlap ratio (OR) of ~44% was obtained. Residues remained at higher scan rates (lower OR values), while CPI damage was observed at lower scan rates (higher OR values) or at two or more scans.

The a-Si:H TSC was fabricated on a CPI film with the following layered structure (from bottom to top, see cross-sectional scanning electron microscopy image in Fig. 1b): CPI substrate, AZO (1 wt% Al, ~400 nm), p^+-a-SiO$_x$:H (5 nm), p-a-SiO$_x$:H (10 nm), p/i interfacial buffer layer (20 nm), i-a-Si:H (280 nm), n-μc-SiO$_x$:H (40 nm), and AZO (600 nm). Fabrication was performed using a multi-chamber cluster composed of PECVD chambers (3 EA) and sputtering chambers (2 EA). The p- and n-layers were deposited using PECVD at a radiofrequency of 13.56 MHz, and the i-layer was deposited using PECVD with a very high frequency of 40.68 MHz. PECVD was carried out at 250 °C using SiH$_4$ and H$_2$ gases for forming the a-Si:H layer and using B$_2$H$_6$, CO$_2$, and PH$_3$ gases for doping this layer. The detailed gas ratios used for film fabrication are listed in Supplementary Table 2. The AZO front and back electrodes were deposited at 150 °C and a DC power of 1000 W using Ar gas. An effective cell area of 0.25 cm^2 was defined by applying a shadow mask for sputtering. The employed fabrication process was reproducible within a certain level of variation. Thirty-two cells on T-CPI (etching time = 2 min) were fabricated, with the distributions of their measured PV parameters shown in Supplementary Fig. 11.

Characterization of CPI and TSCs

Field-emission scanning electron microscopy (JSM-7001F, JEOL) was used to observe the surface of the etched AZO and CPI side transfer to confirm transfer results and compare the texturing degree of both surfaces. Energy-dispersive X-ray spectroscopy was used to analyze the transferred materials on the CPI surface and the residual elements in the sacrificial layer after the laser process. The average, valley-to-valley, and peak-to-valley surface roughnesses of CPI films were measured by AFM (NX10, Park System). The specular and total transmittances of etched AZO, CPI, i-a-Si:H, and n-μc-SiO$_x$:H films as well as the transmittances and reflectances of the fabricated transparent flexible PV cells were measured using ultraviolet-visible (UV-vis) spectrophotometry (Cary 5000, Varian). Optical bandgaps (E_g) were calculated from film transmittances using Tauc plots[48,49]. The dark conductivities (D_c) of i-a-Si:H and n-μc-SiO$_x$:H films were measured using a probe station (MS-TECH) and used to calculate activation energy (E_a) at room temperature[8]. A spectroscopic ellipsometer (SE MG-1000, Nano-view) was used to determine the thicknesses of AZO, p-a-SiO$_x$:H, i-a-Si:H, and n-μc-SiO$_x$:H layers and simulate the refractive indices and extinction coefficients of all layers. EQE was measured using a quantum efficiency measurement system (IQE-200, Newport Co.) to compare the photocurrent generation properties of PV cells. V_{OC}, J_{SC}, FF, and PCE were measured using a solar simulator (Oriel 300, Newport Co.) and a source meter (Keithley 2400) at a power density of 100 mW/cm^2 (1-sun, standard recommended AM1.5 G irradiance) for front and rear incidence operation. For bifacial operation, 1-sun (100 mW/cm^2) and 0.3-sun (~30 mW/cm^2) light sources were used to simultaneously illuminate the front and rear sides, and a white LED source with a diffusion film (LDL90DF, LG; comparable to 0.3-sun condition) was used as the rear light source. The bifacial efficiency (or bifaciality) was defined as the generated maximum output power measured for bifacial operation at a 1-sun incidence power[7,29,50,51].

DATA AVAILABILITY

The datasets generated during and/or analyzed during the current study are available from the corresponding author upon reasonable request.

REFERENCES

1. Peter, S. C. Reduction of CO$_2$ to chemicals and fuels: a solution to global warming and energy crisis. *ACS Energy Lett.* **3**, 1557–1561 (2018).
2. Perera, F. P. Multiple threats to child health from fossil fuel combustion: impacts of air pollution and climate change. *Environ. Health Perspect.* **125**, 141–148 (2017).
3. Gautam, B. R., Li, F. & Ru, G. Assessment of urban roof top solar photovoltaic potential to solve power shortage problem in Nepal. *Energy Build.* **86**, 735–744 (2015).
4. Quan, S. J., Li, Q., Augenbroe, G., Brown, J. & Yang, P. P.-J. A GIS-based energy balance modeling system for urban solar buildings. *Energy Proc.* **75**, 2946–2952 (2015).
5. Wegertseder, P., Lund, P., Mikkola, J. & Alvarado, R. G. Combining solar resource mapping and energy system integration methods for realistic valuation of urban solar energy potential. *Sol. Energy* **135**, 325–336 (2016).
6. Gueymard, C. A. & duPont, W. C. Spectral effects on the transmittance, solar heat gain, and performance rating of glazing systems. *Sol. Energy* **83**, 940–953 (2009).
7. Jo, H. et al. Transparent bifacial a-Si:H solar cells employing silver oxide embedded transparent rear electrodes for improved transparency. *Sol. Energy* **170**, 940–946 (2018).
8. Choi, S. W. et al. P/i interfacial engineering in semi-transparent silicon thin film solar cells for fabrication at a low temperature of 150 °C. *Curr. Appl. Phys.* **19**, 1120–1126 (2019).
9. Park, J. et al. Optimization of laser-patterning process and module design for transparent amorphous silicon thin-film module using thin OMO back electrode. *Sol. Energy* **201**, 75–83 (2020).
10. Khan, M. R., Hanna, A., Sun, X. & Alam, M. A. Vertical bifacial solar farms: physics, design, and global optimization. *Appl. Energy* **206**, 240–248 (2017).
11. Thompson, E. P. et al. Tinted semi-transparent solar panels allow concurrent production of crops and electricity on the same cropland. *Adv. Energy Mater.* **10**, 2001189 (2020).
12. Li, Z. et al. Shading and electric performance of a prototype greenhouse blind system based on semi-transparent photovoltaic technology. *J. Agric. Meteorol.* **74**, 114–122 (2018).
13. Ameen, S., Akhtar, M. S., Seo, H.-K., Nazeeruddin, M. K. & Shin, H.-S. An insight into atmospheric plasma jet modified ZnO quantum dots thin film for flexible perovskite solar cell: optoelectronic transient and charge trapping studies. *J. Phys. Chem. C* **119**, 10379–10390 (2015).
14. Yang, R., Lee, C.-H., Cui, B. & Sazonov, A. Flexible semi-transparent a-Si:H pin solar cells for functional energy-harvesting applications. *Mater. Sci. Eng. B* **229**, 1–5 (2018).
15. Kang, S.-B., Kim, H.-J., Noh, Y.-J., Na, S.-I. & Kim, H.-K. Face-to-face transferred multicrystalline ITO films on colorless polyimide substrates for flexible organic solar cells. *Nano Energy* **11**, 179–188 (2015).
16. Jin, H.-S., Chang, J.-H. & Kim, J.-C. Synthesis and characterization of colorless polyimide nanocomposite films containing pendant trifluoromethyl groups. *Macromol. Res.* **16**, 503–509 (2008).
17. Ni, H., Liu, J., Wang, Z. & Yang, S. A review on colorless and optically transparent polyimide films: chemistry, process and engineering applications. *J. Ind. Eng. Chem.* **28**, 16–27 (2015).
18. Banik, U. et al. Enhancing passive radiative cooling properties of flexible CIGS solar cells for space applications using single layer silicon oxycarbonitride films. *Sol. Energy Mater. Sol. Cells* **209**, 110456 (2020).
19. Fayaz, H., Ahmad, M. S., Pandey, A. K., Rahim, N. A. & Tyagi, V. V. A novel nano-diamond/zinc nanocomposite as potential counter electrode for flexible dye sensitized solar cell. *Sol. Energy* **197**, 1–5 (2020).
20. Shin, C. et al. Control of micro void fraction and optical band gap in intrinsic amorphous silicon thin films (VHF-PECVD) for thin film solar cell application. *Mater. Res. Bull.* **60**, 895–899 (2014).
21. Kim, G., Lim, J. W., Kim, J., Yun, S. J. & Park, M. A. Transparent thin-film silicon solar cells for indoor light harvesting with conversion efficiencies of 36% without photodegradation. *ACS Appl. Mater. Interfaces* **12**, 27122–27130 (2020).
22. Matsui, T. et al. High-efficiency thin-film silicon solar cells realized by integrating stable a-Si:H absorbers into improved device design. *Jpn. J. Appl. Phys.* **54**, 08KB10 (2015).
23. Sai, H., Matsui, T. & Matsubara, K. Stabilized 14.0%-efficient triple-junction thin-film silicon solar cell. *Appl. Phys. Lett.* **109**, 183506 (2016).
24. Lim, J. W., Shin, M., Lee, D. J., Lee, S. H. & Yun, J. S. Highly transparent amorphous silicon solar cells fabricated using thin absorber and high-bandgap-energy n/i-interface layers. *Sol. Energy Mater. Sol. Cells* **128**, 301–306 (2014).
25. Meddeb, H. et al. Novel semi-transparent solar cell based on ultrathin multiple Si/Ge quantum wells. *Prog. Photovolt.* https://doi.org/10.1002/pip.3665 (2022).
26. Söderström, T., Haug, F. J., Terrazzoni-Daudrix, V. & Ballif, C. Optimization of amorphous silicon thin film solar cells for flexible photovoltaics. *J. Appl. Phys.* **103**, 114509 (2008).

27. Meillaud, F. et al. Realization of high efficiency micromorph tandem silicon solar cells on glass and plastic substrates: Issues and potential. *Sol. Energy Mater. Sol. Cells* **95**, 127–130 (2011).

28. Matulionis, I. et al. Semi-transparent amorphous silicon solar cells on inexpensive plastic substrates. *MRS Proc.* **973**, 0973-BB0906-0901 (2006).

29. Shin, M. J. et al. Semitransparent and bifacial ultrathin Cu(In,Ga)Se$_2$ solar cells via a single-stage process and light-management strategy. *Nano Energy* **82**, 105729 (2021).

30. Liang, F. et al. High-performance semitransparent and bifacial perovskite solar cells with MoO$_x$/Ag/WO$_x$ as the rear transparent electrode. *Adv. Mater. Interfaces* **7**, 2000591 (2020).

31. Shin, M. J. et al. Bifacial photovoltaic performance of semitransparent ultrathin Cu(In,Ga)Se$_2$ solar cells with front and rear transparent conducting oxide contacts. *Appl. Surf. Sci.* **535**, 147732 (2021).

32. Hanmandlu, C. et al. Bifacial perovskite solar cells featuring semitransparent electrodes. *ACS Appl. Mater. Interfaces* **9**, 32535–32642 (2017).

33. Chen, D. et al. An efficient TeO$_2$/Ag transparent top electrode for 20%-efficiency bifacial perovskite solar cells with a bifaciality factor exceeding 80%. *J. Mater. Chem. A* **7**, 15156–15163 (2019).

34. Wang, Y. et al. Management of light trapping capability of AZO film for Si thin film solar cells-via tailoring surface texture. *Sol. Energy Mater. Sol. Cells* **179**, 401–408 (2018).

35. Wang, Y. et al. Effective light trapping in thin film silicon solar cells from textured Al doped ZnO substrates with broad surface feature distributions. *Appl. Phys. Lett.* **100**, 263508 (2012).

36. Müller, J., Rech, B., Springer, J. & Vanecek, M. TCO and light trapping in silicon thin film solar cells. *Sol. Energy* **77**, 917–930 (2004).

37. Jiang, Q. et al. Texture surfaces and etching mechanism of ZnO:Al films by a neutral agent for solar cells. *Sol. Energy Mater. Sol. Cells* **130**, 264–271 (2014).

38. Wilken, K. et al. Nanoimprint texturing of transparent flexible substrates for improved light management in thin-film solar cells. *Phys. Status Solidi RRL* **9**, 215–219 (2015).

39. Wang, B.-Y. et al. Enhanced light scattering and trapping effect of Ag nanowire mesh electrode for high efficient flexible organic solar cell. *Small* **11**, 1905–1911 (2015).

40. Söderström, K. et al. UV-nano-imprint lithography technique for the replication of back reflectors for n-i-p thin film silicon solar cells. *Prog. Photovolt.* **19**, 202–210 (2011).

41. Wright, J. G. Jr, Schmidt, H. & Hawkins, A. R. Effects of post-etch microstructures on the optical transmittance of silica ridge waveguides. *J. Lightwave Technol.* **38**, 6280–6285 (2020).

42. Yoo, J. et al. High transmittance and low resistive ZnO:Al films for thin film solar cells. *Thin Solid Films* **480–481**, 213–217 (2005).

43. Li, L. et al. Angular dependence of multiangle dynamic light scattering for particle size distribution inversion using a self-adapting regularization algorithm. *J. Quant. Spectrosc. Radiat. Transf.* **209**, 91–102 (2018).

44. Hassanien, A. S. & Akl, A. A. Optical characterizations and refractive index dispersion parameters of annealed TiO$_2$ thin films synthesized by RF-sputtering technique at different flow rates of the reactive oxygen gas. *Phys. B Condens. Matter* **576**, 411718 (2020).

45. Zhu, F. & Singh, J. An approach to study the effect of the band tail widths on the photovoltaic performance of p-i-n a-Si: H solar cells. *J. Non-Cryst. Solids* **163**, 65–73 (1993).

46. Schiff, E. A. Low-mobility solar cells: a device physics primer with application to amorphous silicon. *Sol. Energy Mater. Sol. Cells* **78**, 567–595 (2003).

47. Liang, J., Schiff, E. A., Guha, S., Yan, B. & Yang, J. Hole-mobility limit of amorphous silicon solar cells. *Appl. Phys. Lett.* **88**, 63512 (2006).

48. Tauc, J. Optical properties and electronic structure of amorphous Ge and Si. *Mater. Res. Bull.* **3**, 37–46 (1968).

49. Davis, E. A. & Mott, N. F. Conduction in non-crystalline systems V. Conductivity, optical absorption and photoconductivity in amorphous semiconductors. *Philos. Mag.* **22**, 903–922 (1970).

50. Imran, H. et al. High-performance bifacial perovskite/silicon double-tandem solar cell. *IEEE J. Photovolt.* **8**, 1222–1229 (2018).

51. Ding, J. et al. Improvement of light trapping in bifacial PERC silicon solar cells by optimizing the rear surface morphology. *ACS Appl. Energy Mater.* **5**, 5875–5885 (2022).

ACKNOWLEDGEMENTS

AUTHOR CONTRIBUTIONS

S.-W.C. contributed to the preparation of the draft as the first author and proceeded with the optical simulation; J.-H.P. and J.-W.S. contributed to the device fabrication; C.M. and Y.K. contributed to measurements and post-experiments for the supporting information; P.S. contributed to advisory works for the fabrication; M.S. contributed advisory works for the research proposal and preparing the manuscript; J.-D.K. contributed as a supervisor for the research

COMPETING INTERESTS

The authors declare no competing interests.

ADDITIONAL INFORMATION

Supplementary information The online version contains supplementary material available at https://doi.org/10.1038/s41528-023-00251-6.

Correspondence and requests for materials should be addressed to Pungkeun Song, Myunghun Shin or Jung-Dae Kwon.

Reprints and permission information is available at http://www.nature.com/reprints

Publisher's note Springer Nature remains neutral with regard to jurisdictional claims in published maps and institutional affiliations.